JACS
JOURNAL OF THE AMERICAN CHEMICAL SOCIETY
pubs.acs.org/JACS
Article

Light-Induced Selective Hydrogenation over PdAg Nanocages in Hollow MOF Microenvironment

Luyan Li, Yanxiao Li, Long Jiao, Xiaoshuo Liu, Zhentao Ma, Yu-Jia Zeng,* Xusheng Zheng, and Hai-Long Jiang*

Cite This: J. Am. Chem. Soc. 2022, 144, 17075−17085
Read Online
ACCESS | Metrics & More | Article Recommendations | Supporting Information

ABSTRACT: Selective hydrogenation with high efficiency under ambient conditions remains a long-standing challenge. Here, a yolk−shell nanostructured catalyst, PdAg@ZIF-8, featuring plasmonic PdAg nanocages encompassed by a metal−organic framework (MOF, namely, ZIF-8) shell, has been rationally fabricated. PdAg@ZIF-8 achieves selective (97.5%) hydrogenation of nitrostyrene to vinylaniline with complete conversion at ambient temperature under visible light irradiation. The photothermal effect of Ag, together with the substrate enrichment effect of the catalyst, improves the Pd activity. The near-field enhancement effect from plasmonic Ag and optimized Pd electronic state by Ag alloying promote selective adsorption of the $-NO_2$ group and therefore catalytic selectivity. Remarkably, the unique yolk−shell nanostructure not only facilitates access to PdAg cores and protects them from aggregation but also benefits substrate enrichment and preferential $-NO_2$ adsorption under light irradiation, the latter two of which surpass the core−shell counterpart, giving rise to enhanced activity, selectivity, and recyclability.

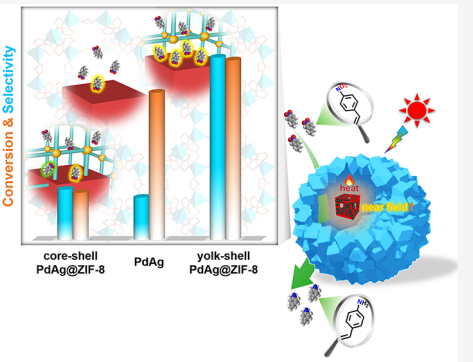

INTRODUCTION

Chemoselective hydrogenation of nitroaromatics is of great importance in the production of the corresponding aniline derivatives. Particularly, chemoselective hydrogenation of nitroaromatics with other reducible groups, such as carbon−carbon double or triple bonds, is a class of important reactions in modern industry. The produced functionalized anilines are significant industrial intermediates for the synthesis of pharmaceuticals, polymers, herbicides, and fine chemicals.[1−7] The Pd-based catalysts, with excellent hydrogen and nitroaromatics activation capacity, have been intensively reported to catalyze the hydrogenation of nitrocompounds.[8−13] However, related reactions usually suffer from harsh catalytic conditions such as high H_2 pressure (>3 bar) or temperature (>343 K).[10−13] Moreover, it remains challenging to promote selective nitro hydrogenation in the presence of other reducible groups since the nitro and other unsaturated groups are hardly distinguished by Pd sites.[10−13] Therefore, the alternative catalytic systems that selectively produce functionalized anilines under mild conditions are highly pursued.

To alleviate the high reaction temperature, using solar energy instead of traditional heat to drive the reaction would be favorable based on the localized surface plasmon resonance (LSPR) properties of metal nanocrystals.[14−16] The common LSPR metals, such as Au, Ag and Cu, possess high carrier density and display good solar spectrum absorption from the ultraviolet (UV) to the near-infrared (NIR) region, capable of converting light to heat.[17−22] Among them, the well-developed Ag nanocubes (NCs) presenting high stability and intense absorption in the visible region are very promising.[23,24] Given that Ag NCs are less active metal with limited ability to activate H_2, the introduction of other active sites, such as Pd sites, forming PdAg nanoparticles (NPs) might be an effective strategy to the integration of their respective advantages. It is expected that the creation of heat energy surrounding active Pd sites would greatly promote the hydrogenation process under light irradiation.

On account of the high surface energy, small PdAg NPs are prone to aggregate especially under irradiation or heating in the reaction. To protect them from aggregation, the isolation of them into nanoreactors encompassed by porous materials with proper pore sizes, affording yolk−shell nanostructures, should be a promising strategy. The porous shell will allow the transfer of substrates/products and guarantee the accessibility of Pd active sites. The reaction nanospace might enable H_2 and substrate enrichment for enhanced activity.[25] Against this backdrop, metal−organic frameworks (MOFs),[26−31] a class of crystalline porous materials featuring uniform pores and good

Received: June 26, 2022
Published: September 7, 2022

Downloaded via UNIV SCIENCE AND TECHNOLOGY CHINA on September 23, 2022 at 03:26:49 (UTC).
See https://pubs.acs.org/sharingguidelines for options on how to legitimately share published articles.

ACS Publications
© 2022 American Chemical Society

https://doi.org/10.1021/jacs.2c06720
J. Am. Chem. Soc. 2022, 144, 17075−17085

heat insulation capability,[32] would be ideal shells for PdAg NPs.[33−39]

With the above mentioned factors in mind, the PdAg nanocages are encapsulated into a representative MOF, Zn(2-methylimidazole)$_2$ (ZIF-8),[40,41] by means of Cu_2O sacrificial templates to create the hollow space, affording PdAg@ZIF-8 with a yolk−shell structure (Scheme 1). The PdAg nanocages

Scheme 1. Synthetic Route for the Yolk−Shell PdAg@ZIF-8 Composite

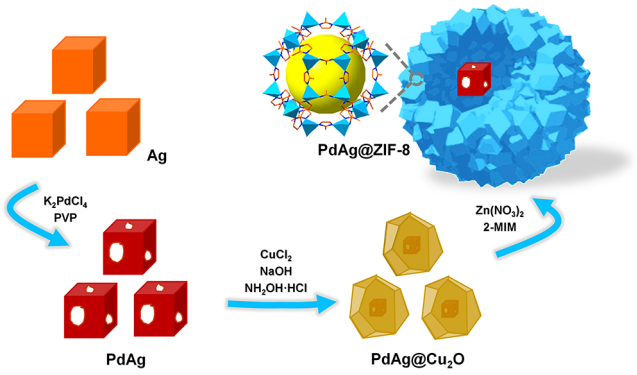

integrate the excellent LSPR properties of Ag, exhibiting a broad plasmonic band in the UV−vis spectral range for efficient photothermal conversion and near-field enhancement and the high activity of Pd species. As a result, the yolk−shell PdAg@ZIF-8 composite displays excellent hydrogenation of nitrostyrene to aminostyrene with very high selectivity (97.5%) in ethanol at ambient temperature under visible light irradiation in the presence of NH_3BH_3 as the hydrogen source. The ZIF-8 shell not only allows the free transport of reactants and products but also isolates the PdAg nanocages from aggregation, thereby guaranteeing recyclability. Remarkably, the unique hollow space between the PdAg core and the MOF shell not only allows sufficient exposure of active sites but also facilitates substrate enrichment and preferential $-NO_2$ group adsorption under light irradiation, significantly improving the conversion and selectivity, with reference to the core−shell structure and other corresponding counterparts.

RESULTS AND DISCUSSION

The yolk−shell PdAg@ZIF-8 nanostructure was fabricated by several procedures. First, monodispersed Ag NCs with a uniform size of ∼50 nm were successfully synthesized following a modified polyol protocol (Figures 1a and S1).[42,43] Then, K_2PdCl_4 was introduced, and the Ag NCs were converted to PdAg nanocages through the spontaneous galvanic replacement (E°_{Ag/Ag^+} = +0.80 eV vs SHE; $E^\circ_{Pd/Pd^{2+}}$ = +0.95 eV vs SHE) (Figure S2).[43] Transmission electron microscopy (TEM) images clearly illustrate that PdAg nanocages (∼50 nm) with a hollow structure inherit the sizes of Ag NCs (Figure 1b). The frames of original Ag nanocubes remain intact in the evolution process with pinholes randomly formed on the side faces, and a more porous morphology is obtained with increased Pd content (Figure S3). Moreover, powder X-ray diffraction (XRD) of PdAg nanocages displays two peaks at 38.4 and 44.7°, which locate between the standard peaks of Ag and Pd, suggesting the formation of PdAg alloys, according to the Vegard's law (Figure S4), in accordance with the high-resolution TEM (HRTEM) observation with a lattice fringe of 1.96 Å, a value falling in between Pd(100) and Ag(100) (Figure 1c). To verify the alloy structure of PdAg, the synchrotron radiation photoemission spectroscopy (SRPES) spectra of Pd 3d and Ag 3d are investigated with photon energies of 470, 670, 970, and 1486.6 eV, respectively. The steady atomic fraction of Ag and Pd clearly points to the alloy structure with the Pd/Ag atomic ratio of ∼1:9 (Figure 1e), in line with the inductively coupled plasma atomic emission spectroscopy (ICP-AES) results for the PdAg nanocages. Moreover, this alloy structure can be further supported by the elemental mapping of Ag and Pd, in which the presence of Ag is accompanied by Pd in the whole nanocage (Figure 1f).

To synthesize the yolk−shell nanostructure, the obtained PdAg nanocages were coated with Cu_2O to give PdAg@Cu_2O with a core−shell structure, followed by further assembly of ZIF-8 on the external surface. The Cu_2O was mostly etched off by the protons *in situ* generated during the growth of the ZIF-8 shell and further could be completely removed by soaking in methanol containing 3% ammonium hydroxide,[44] releasing out the hollow space between the PdAg nanocage and ZIF-8 and accordingly affording the yolk−shell PdAg@ZIF-8 composite. According to the TEM results, the Cu_2O shell is ∼78 nm in thickness and coated on PdAg nanocages, giving PdAg@Cu_2O of ∼206 nm (Figure S5). TEM observation of PdAg@ZIF-8 with sizes of 350−450 nm clearly demonstrates its yolk−shell structure, where the cubic shape and the hollow structure of PdAg nanocages inside are well retained (Figures 1d and S6). The hollow space of ∼200 nm in the yolk−shell structure almost matches the above PdAg@Cu_2O particle sizes, perfectly supporting its template role of Cu_2O. Moreover, the presence of macropores in the yolk−shell PdAg@ZIF-8 is also confirmed by the mercury intrusion method (Figure S6b). Upon ZIF-8 coating and ammonium hydroxide etching, the powder X-ray diffraction pattern (XRD) peaks of Cu_2O in PdAg@ZIF-8 disappear (Figure S4), revealing the Cu_2O removal, which is further approved by the absence of Cu signal in the ICP-AES analysis, together with the elemental mapping analysis and X-ray photoelectron spectroscopy (XPS) results (Figure S7). The characteristic diffraction peaks of yolk−shell PdAg@ZIF-8 demonstrate the high crystallinity of the ZIF-8 shell, whereas no evident diffraction can be indexed to metal species (2θ = 35−60°), possibly due to the low loading of PdAg nanocages (Figure S4). The contents of Ag and Pd in PdAg@ZIF-8 are estimated to be 1.6 and 0.17 wt %, respectively, based on the ICP-AES data (Figure S7).

Nitrogen sorption experiments indicate that PdAg@ZIF-8 inherits the high porosity, the type-I behavior, and the micropore feature of the parent ZIF-8 (Figures 2a and S8). Its Brunauer−Emmett−Teller (BET) surface area is estimated to be 1035 m^2/g, a slight decrease compared with ZIF-8 (1254 m^2/g) caused by the PdAg incorporation. X-ray photoelectron spectroscopy (XPS) spectra show that the Pd $3d_{5/2}$ peak of PdAg nanocages shifts to the lower binding energy than that of pure Pd, indicating the electron transfer from Ag to Pd due to the low electronegativity of Ag (Figure 2b).[45] The UV−Vis spectrum of PdAg displays a broad peak at ∼450 nm, which is inherited to PdAg@ZIF-8 with broad adsorption in the range of 300−600 nm (Figure 2c). Given the good light-harvesting ability of PdAg@ZIF-8 based on the UV−vis results, its photothermal effect has been examined. The temperatures of the ethanol solution in the absence of additive or the presence of PdAg nanocages, PdAg@ZIF-8, and the control sample were

https://doi.org/10.1021/jacs.2c06720
J. Am. Chem. Soc. 2022, 144, 17075−17085

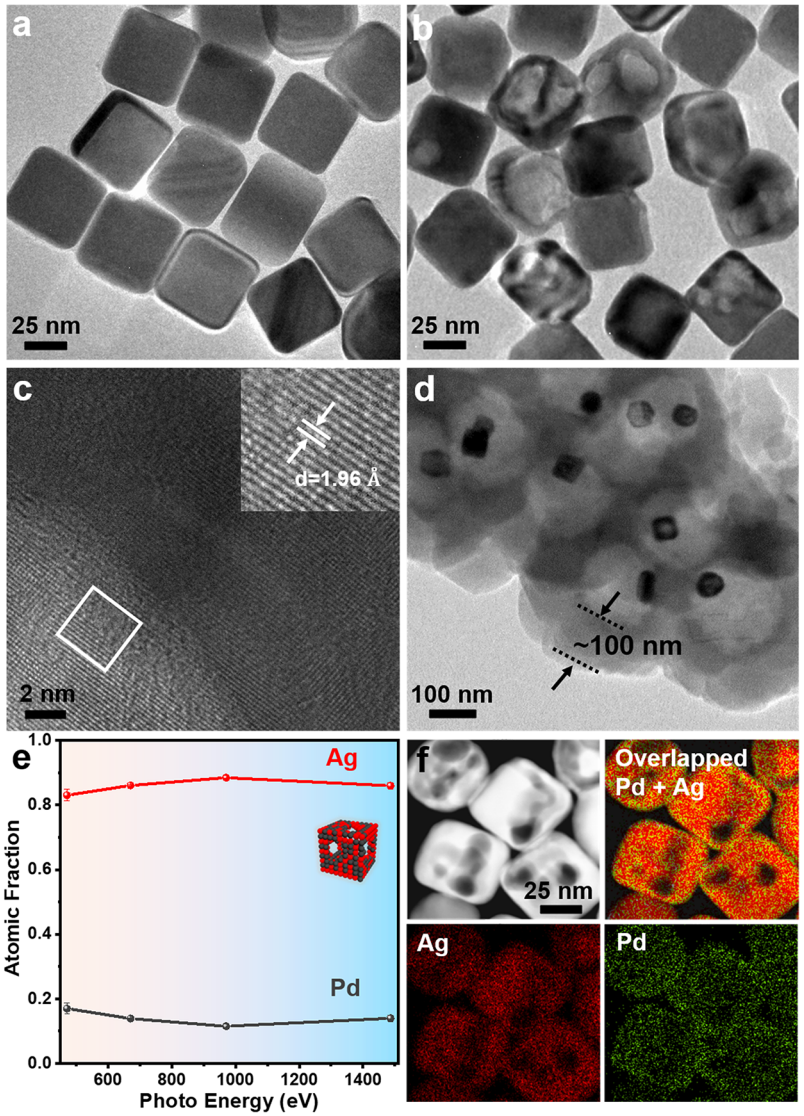

Figure 1. (a) TEM image of Ag NCs. (b) TEM and (c) HRTEM images of PdAg nanocages (inset of c: lattice fringe of PdAg). (d) TEM image of the yolk−shell nanostructured PdAg@ZIF-8 composite. (e) Dependence of Ag and Pd atomic fractions for the PdAg nanocages as a function of photon energy. (f) High-angle annular dark-field scanning transmission electron microscopy (HAADF-STEM) of PdAg nanocages and the corresponding elemental mapping of Ag (red), Pd (green), and their overlapping.

examined under light irradiation (λ > 400 nm) (Figure 2d). It slowly increases and rises by 10 °C in the blank solution after 30 min of irradiation, which is possibly due to the NIR thermal effect. The temperature change is very similar to that with ZIF-8 in the solution. Remarkably, both the naked PdAg nanocages and PdAg@ZIF-8 display a significant temperature increment of up to ∼28 °C in the solution, reflecting the importance of PdAg with the LSPR effect (Figure 2d).

Encouraged by the results above, the hydrogenation of *para*-nitrostyrene, which is a catalytically endothermic process with a very challenging task of specifically reducing the nitro to amino group in the presence of C═C bonds, has been investigated over the yolk−shell PdAg@ZIF-8 (Figure 3a and Table S1). To avoid the most common high pressure of H_2 for this reaction, ammonia borane (NH_3BH_3) was employed as an alternative instead of H_2,[46,47] given its high hydrogen content (19.6 wt %) and excellent solubility in alcohol to produce hydrogen.[48−50] The alcoholysis of NH_3BH_3 over PdAg@ZIF-8 is able to produce H_2, and the activity can be improved under light irradiation (Figure S9). Inspired by the results, the hydrogenation of *para*-nitrostyrene has been carried out. The reaction gives a little bit conversion to nitroethylbenzene in the absence of a catalyst or the presence of ZIF-8. The very low conversion might be contributed by the thermal effect from the lamp, which could accelerate the decomposition of NH_3BH_3 to reduce the substrate. To our delight, the quantitative conversion of *para*-nitrostyrene and 97.5% selectivity to *para*-aminostyrene are achieved by PdAg@ZIF-8 within 20 min under light irradiation (Figure 3a). Strikingly, the reaction selectivity can be maintained, and no overhydrogenation occurred even the reaction time is extended to 3 h (Figure S10). By comparing the results between ZIF-8 and yolk−shell PdAg@ZIF-8, it is apparent that PdAg nanocages serve as active sites in this hydrogenation process. However, to our delight, compared with PdAg@ZIF-8, a reduced activity is observed when PdAg nanocages are directly used in the reaction with other conditions being fixed (Figure 3a and Table S1, entries 1 and 2). This comparison suggests that the

https://doi.org/10.1021/jacs.2c06720
J. Am. Chem. Soc. 2022, 144, 17075−17085

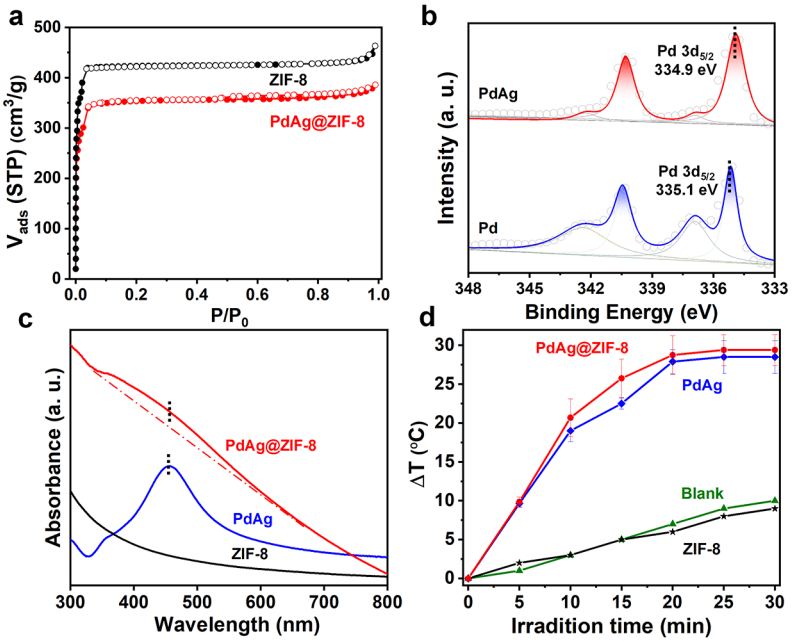

Figure 2. (a) Nitrogen sorption isotherms for ZIF-8 and PdAg@ZIF-8 at 77 K. (b) XPS spectra of Pd 3d in PdAg nanocages and Pd nanoparticles. (c) UV−vis adsorption spectra for PdAg nanocages, ZIF-8, and yolk−shell PdAg@ZIF-8. (d) Temperature variation of the reaction solution along with the light irradiation in the blank or in the presence of PdAg@ZIF-8, ZIF-8, and PdAg.

ZIF-8 shell is beneficial to the conversion, which can be explained by several possible reasons: (1) The physical protection of the ZIF-8 shell for PdAg nanocages does not cause transport limitation (Figure S11) but prevents PdAg from aggregation. As demonstrated by TEM results (Figure S12), severe agglomeration of PdAg nanocages takes place in the catalytic process in the absence of ZIF-8. (2) The particular nanoreactor microenvironment created by the ZIF-8 shell for substrate enrichment.[51−53] (3) The thermal insulation effect of ZIF-8.[32] This restrains the heat effect inside the hollow space encompassed by the MOF shell, thereby promoting the reaction.

Light irradiation plays a significant role in the (particularly endothermic) reactions with plasmonic metal-involved catalysts based on previous reports.[20,33] To verify the influence of light irradiation wavelength in this work, the reaction has been implemented under different irradiation conditions (Figure 3a and Table S1, entries 3−4). Compared to the catalytic performance under λ > 400 nm, a comparable catalytic performance is obtained under the full spectrum and a slight decrease of catalytic performance is observed under irradiation >450 nm that is partly involved in the UV−Vis adsorption of PdAg nanocages. Therefore, the current wavelength range (λ > 400 nm) would be the optimal condition from the view of energy saving and reaction efficiency. To further figure out the role of light irradiation, the reaction under dark conditions is also carried out (Figure 3a and Table S1, entry 5). As expected, only 47% of the substrate is converted with a low selectivity of 68% to *para*-aminostyrene under identical conditions except for no irradiation (Figure 3a). In fact, as observed above (Figure 2d), an apparent increase of temperature in the solution is observed during the catalysis under visible light irradiation. The accurate temperature increase from 28.5 to 59.3 °C in the reaction solution has been recorded on a thermograph (Figure 3b). It is worth noting that the real temperature around PdAg sites should be much higher than the detected values in the reaction solution due to the thermal diffusion difficulty hampered by the MOF,[32] and the large amount of solution in the system being hardly heated by the hot "spots" of PdAg nanocages. To support this conjecture, the control reaction was carried out by heating at 60 °C in an oil bath instead of light irradiation (Figure 3a and Table S1, entry 6). Unfortunately, the conversion reaches 84.4% with 72% selectivity to the targeted product. Upon elevating the temperature to 80 °C, a comparable activity is observed (Table S1, entry 7). This result reflects that the temperature of the PdAg interface is higher than 60 °C and possibly ∼80 °C under light irradiation. Moreover, the reduced selectivity under heat conditions indicates that the light also benefits the selective hydrogenation of the $-NO_2$ group (Table S1, entries 6 and 7), which is probably due to the generated near-field enhancement, promoting the selective adsorption, as discussed below.[54,55]

To better understand the functions and impacts of each component in the catalytic system, a series of control experiments have been conducted (Table 1). The monometallic Ag@ZIF-8 and Pd@ZIF-8, featuring similar yolk−shell structures to PdAg@ZIF-8, were synthesized for the same reaction (Figure S13). Due to the poor ability of Ag on H_2 activation, Ag@ZIF-8 gave only half conversion of nitrostyrene with bad selectivity (entries 1 and 2). In comparison, Pd@ZIF-8 displays a 100% conversion yet >99% selectivity to the overhydrogenated aminoethylbenzene (entry 3), reflecting that Pd is the main active site. The commercial Pd/C displays similar performance to that of Pd@ZIF-8 (entries 4 and 5), where the overhydrogenation reveals the importance of Ag species. The presence of Ag regulates the Pd electronic state, as demonstrated by the XPS results above (Figure 2b), which effectively prevents the overhydrogenation and significantly improves the selectivity to the targeted product vinylaniline. To further verify this point, the Pd content increases from the original 9.6 to 29.5 wt % in PdAg nanocages to afford yolk−

https://doi.org/10.1021/jacs.2c06720
J. Am. Chem. Soc. 2022, 144, 17075−17085

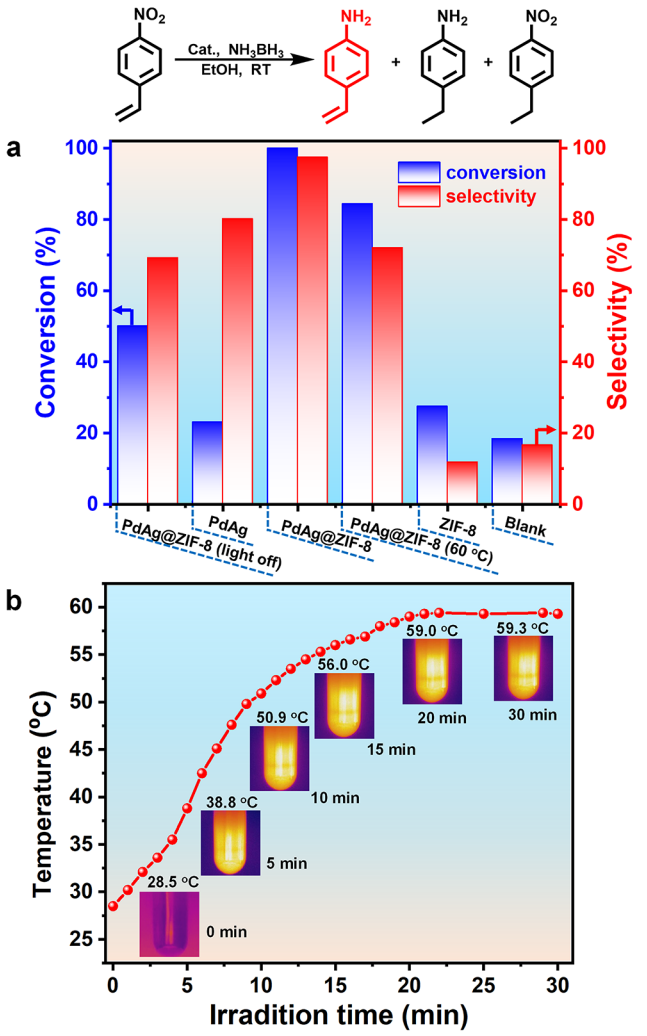

Figure 3. (a) Chemoselective hydrogenation of *para*-nitrostyrene over different catalysts. Reaction conditions: 5.5 mg of catalyst (totally 0.1 mg of Ag and Pd in each catalyst), 0.1 mmol of nitrostyrene, 5 mL of ethanol, 15 mg of NH_3BH_3, 20 min of reaction time length, light irradiation (λ > 400 nm, 300 mW/cm^2) at ambient temperature. (b) Time-dependent temperature detected for the reaction solution under visible light irradiation (λ > 400 nm). The thermograph recorded the real-time temperature of the reaction tube at different time intervals.

shell Pd_3Ag_7@ZIF-8. As expected, an increased percentage (7.0%) of overhydrogenated aminoethylbenzene is observed in catalytic products (entries 6 and 7), with reference to the 2.5% selectivity of aminoethylbenzene achieved by the optimized yolk−shell PdAg@ZIF-8 (entries 8 and 9). Notably, the excellent catalytic activity (>99%) and selectivity (97.5%) of yolk−shell PdAg@ZIF-8 toward the hydrogenation of nitrostyrene are among the highest level in metal-based catalysts reported recently (Table S2).

To investigate the influence brought by the cavity (nanoreactor) in the yolk−shell structure, the core−shell structured PdAg@ZIF-8 composite, PdAg/C, PdAg/SiO_2, and PdAg/Al_2O_3, have been deliberately fabricated as controls. To our surprise, in sharp contrast to the yolk−shell PdAg@ZIF-8, the resulting core−shell counterpart and the supported catalysts, even involving PdAg nanocages, display much inferior activity (Table 1, entries 10−14). This comparison unambiguously speaks for the importance of a hollow microenvironment

Table 1. Catalytic Hydrogenation of Nitrostyrene over Diverse Catalysts

			sel. (%)[a]		
entry	catalyst	con. (%)	*a*	*b*	*c*
1	Ag@ZIF-8	50.0	63.6	14.1	22.3
2[b]	Ag@ZIF-8	84	60	21	19
3	Pd@ZIF-8	100	<1	>99	
4[c]	Pd@ZIF-8	85	<1	>99	
5[c]	Pd/C	85	<1	>99	
6	Pd_3Ag_7@ZIF-8	100	93.0	7.0	
7[d]	Pd_3Ag_7@ZIF-8	85	94.0	6.0	
8	PdAg@ZIF-8	100	97.5	2.5	
9[e]	PdAg@ZIF-8	85	97.5	2.5	
10	core−shell PdAg@ZIF-8	27.4	25.7	24.7	49.6
11[f]	core−shell PdAg@ZIF-8	83	21	64	15
12	PdAg/C	18	89	3	8
13	PdAg/SiO_2	20	90	5	5
14	PdAg/Al_2O_3	19	88	7	5

[a]Reaction conditions: 5.5 mg of catalyst (totally 0.1 mg of Ag and Pd in each catalyst), 0.1 mmol of nitrostyrene, 5 mL of ethanol, 15 mg of NH_3BH_3, 20 min, λ > 400 nm, 300 mW/cm^2 at ambient temperature. [b]25 min. [c]3 min. [d]15 min. [e]17 min. [f]60 min. Catalytic reaction products analyzed and identified by gas chromatography.

around the active centers in the yolk−shell nanostructure, which might enable effective enrichment of substrates and maximum accessibility of active sites. Moreover, the core−shell PdAg@ZIF-8 gives much decreased selectivity (entries 10 and 11), which may be attributed to the restricted substrate rotation on the PdAg surface by the narrow pore size of the ZIF-8 shell (3.4 Å), as further discussed below.

To further understand the high selectivity achieved with outstanding catalytic performance of yolk−shell PdAg@ZIF-8, the diffuse reflectance infrared Fourier transform spectroscopy (DRIFTS) experiments, involving the mixture of nitrobenzene and styrene, have been resorted to examine its substrate adsorption behavior. The peaks at 1530 and 1348 cm^{-1} ascribed to the nitro (−NO_2) group and at 1630 cm^{-1} assigned to the carbon−carbon double bond (−C=C) group are observed for the yolk−shell PdAg@ZIF-8, whereas no apparent signal is present with ZIF-8 (Figure S14). The results indicate that nitrobenzene and styrene can be adsorbed on PdAg sites instead of the MOF. Notably, although both adsorbate signals can be found over PdAg@ZIF-8, the band of the adsorbed −NO_2 group remains with much stronger intensity than that of the −C=C group. In contrast, the similar adsorption intensity of the −NO_2 group and −C=C group is observed on the Pd surface in Pd@ZIF-8 (Figure S14). This reveals the preferential adsorption of the −NO_2 group on PdAg nanocages, accounting for the very high selectivity in the hydrogenation of *para*-nitrostyene over PdAg@ZIF-8. Density functional theory (DFT) calculation results indicate that the adsorption energy of the −NO_2 group (-0.57 eV) over PdAg is much higher than that of the −C=C group (−0.07 eV) (Figure S15), probably due to the high electronegativity of PdAg nanocage, benefiting the polar −NO_2 group adsorption.[10]

https://doi.org/10.1021/jacs.2c06720
J. Am. Chem. Soc. 2022, 144, 17075−17085

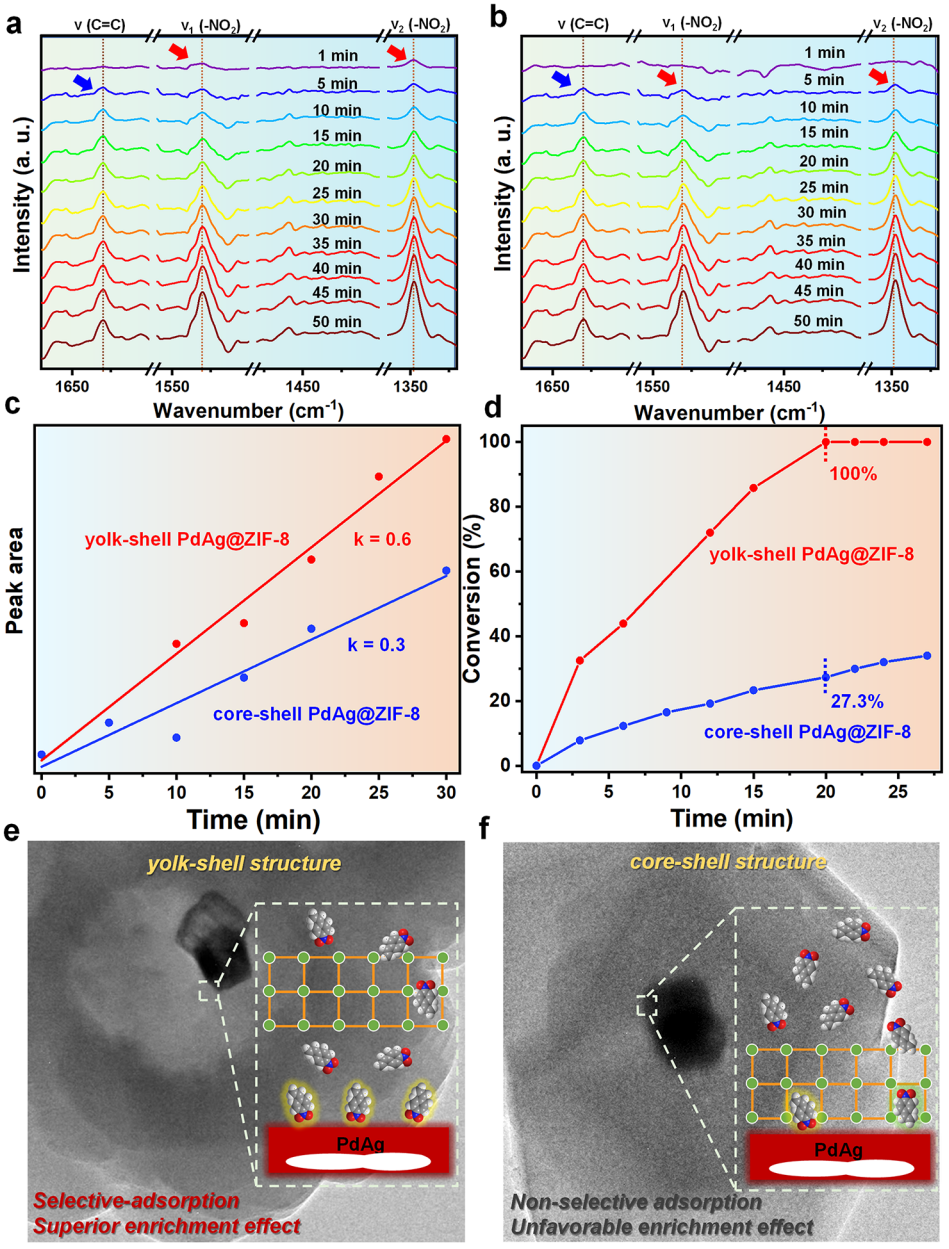

Figure 4. Time-dependent DRIFTS intensity for nitrobenzene and styrene mixture over the (a) yolk−shell or (b) core−shell PdAg@ZIF-8 catalysts under light irradiation. (c) Enrichment rate for nitrobenzene and styrene mixture over the yolk−shell and core−shell PdAg@ZIF-8 based on the data of the value of their adsorption area from (a, b). (d) Time-dependent conversion in the hydrogenation of *para*-nitrostyrene using the yolk−shell or core−shell PdAg@ZIF-8 catalysts. Schematic diagram showing the distinctly different substrate adsorption and enrichment effects with the (e) yolk−shell or (f) core−shell PdAg@ZIF-8.

To further gain insight into the adsorption process, time-dependent competitive adsorption experiments have also been conducted. Notably, the yolk−shell PdAg@ZIF-8 exhibits main sharp peaks at 1530 and 1348 cm^{-1} related to the $-NO_2$ group appearing at 1 min, whereas the peak of the −C═C group becomes discernible at 5 min under light irradiation (Figure S16), supporting the selective hydrogenation of the $-NO_2$ group (Figure 3a). Inversely, without light irradiation, the signals of the $-NO_2$ group cannot be found until 20 min, while the appearance of the −C═C group adsorption remains at 5 min (Figure S16). Apparently, the introduction of light irradiation plays a key role in the selective adsorption of the $-NO_2$ group. Moreover, even after saturated adsorption, the lower peak intensity of the $-NO_2$ group in the dark than that under light irradiation is observed, whereas no increased signal intensity of the −C═C group is found under light irradiation (Figure S17a).

In comparison, the signals of both the $-NO_2$ group and −C═C group do not give an apparent increase over Pd@ZIF-8 upon light irradiation (Figure S17b). The results unambiguously demonstrate that the generated enhanced electromagnetic field effect caused by the Ag species in PdAg nanocages plays a vital role on the preferential adsorption of the $-NO_2$ group under light irradiation (Figure S16). Moreover, the concentration change of nitrobenzene and styrene in ethanol under light on or off conditions has also

https://doi.org/10.1021/jacs.2c06720
J. Am. Chem. Soc. 2022, 144, 17075−17085

been detected (Figure S18). Under light off conditions, nitrobenzene adsorption gives ∼15% concentration decrease, while styrene presents an ∼10% concentration change in the reaction solvent, indicating that nitrobenzene has a strong interaction with PdAg@ZIF-8, in accordance with the DFT calculation (Figure S15). Strikingly, upon light irradiation, the concentration of nitrobenzene in the solvent significantly decreases from 85 to 57%, suggesting that nitrobenzene interacts with PdAg@ZIF-8, probably due to the generated electromagnetic field around PdAg induced by light, in line with the DRIFTS result (Figure S17a). By contrast, the concentration of styrene has no apparent change under light on and off conditions due to its weak interaction with PdAg@ZIF-8.

In addition, the molecular polarizability of the substrate has a significant effect on the interaction between the substrate molecules and PdAg alloys, according to the previous reports.[55−57] It is reported that the high molecular polarizability contributes to the strong response to the optical plasmon field on the alloy surface.[55] Therefore, to further understand the interaction difference between $-NO_2$ and −C═C groups on the PdAg surface, the polarizability of both groups is evaluated via root mean square error (RMSE) of mulliken charge (Figure S19). The results suggest that the higher RMSE of mulliken charge on the $-NO_2$ group (0.35) than that of the −C═C (0.18), illustrating the higher polarizability of the $-NO_2$ group, which is probably easily trapped by the plasmon field on the PdAg surface.[55] It can be concluded that the light-induced near-field enhancement around PdAg is beneficial to the preferential adsorption of the $-NO_2$ group that displays a high polarizability than that of the −C═C group, together with the optimized Pd electronic state by Ag alloying (Figure 2b), accounting for the resulting high selectivity.[55,58,59]

Furthermore, compared to the preferential adsorption of the $-NO_2$ group at 1 min over the yolk−shell PdAg@ZIF-8 (Figure 4a), the PdAg nanocages present the adsorption signals of the $-NO_2$ group at 7 min and the peak of −C═C adsorption appears at 10 min (Figure S20) under light irradiation. The results unambiguously demonstrate that the yolk−shell catalyst possesses substrate enrichment ability for the adsorbates, and its selective adsorption on the $-NO_2$ group is inherited from PdAg nanocages and even further enhanced. In comparison to yolk−shell PdAg@ZIF-8, the signals of $-NO_2$ and −C═C groups appear simultaneously at 5 min for the core−shell PdAg@ZIF-8 (Figure 4b), suggesting the weak enrichment effect in the core−shell PdAg@ZIF-8 and the absence of selective adsorption for both substrates under light irradiation. It is assumed that the hollow space inside the yolk−shell structure, which is unhindered for substrate rotation, creates favorable conditions for selective adsorption of the $-NO_2$ group. In sharp contrast, the small aperture size of ZIF-8 around PdAg in the core−shell structure impedes the random rotation of the substrates, unfavorable to the selective adsorption of the $-NO_2$ group.[60] Moreover, the enrichment rate of the yolk−shell and core−shell PdAg@ZIF-8 for the substrate has been evaluated to understand their differentiated activity increase compared to PdAg nanocages in the reaction. According to the adsorption peak area change of −C═C and $-NO_2$ groups along with time (Figure 4a,b), the yolk−shell PdAg@ZIF-8 displays a superior enrichment effect (k = 0.6) for the substrate to the core−shell one (k = 0.3), accounting for the higher activity of yolk−shell PdAg@ZIF-8 (Figures 4c and S21). This is in good line with the kinetic curves of the reaction over these two catalysts, where the conversion over the yolk−shell PdAg@ZIF-8 is completed within 20 min, while only 27.3% conversion is obtained at the same time over the core−shell PdAg@ZIF-8 (Figures 4d and S22). As far as we know, this is the first work providing direct and explicit DRIFTS evidence on the particular advantages with regard to the hollow microenvironment in the yolk−shell nanostructure on selective adsorption and enrichment of substrates, which are responsible for the high selectivity and activity, surpassing its core−shell counterpart (Figure 4e,f).

Inspired by the remarkable catalytic performance of yolk−shell PdAg@ZIF-8 in selective hydrogenation of *para*-nitrostyrene, the most common hydrogen source, H_2, has also been applied to investigate the hydrogenation process (Table S3). Unfortunately, the reaction activity sharply decreases with H_2 gas due to its poor solubility in EtOH. Moreover, the selectivity gives an apparent decrease using H_2 instead of NH_3BH_3. The results indicate that NH_3BH_3 is crucial for both activity and selectivity in the reaction. To further approve this point, deuterium-labeling experiments are conducted (Figure S23). After introducing the NH_3BD_3 into the reaction, the KIE value (K_L/K_H, K is the reaction rate) is 3, falling into the range (2−7) of the primary kinetic isotope effect.[61] This result indicates that the cleavage of the B−H bond generating H^- species is involved in the rate-determining step, and the H^- species might directly cooperate with the $-NO_2$ group or −C═C group in *para*-nitrostyrene.[62] However, it is reported that the generated polar H^- species has a weak interaction with the −C═C bond,[62,63] which could suppress the hydrogenation of the −C═C bond in *para*-nitrostyrene, leading to the high selectivity.

The stability investigation for the yolk−shell PdAg@ZIF-8 indicates that the high activity and selectivity of the catalyst can be maintained well in the five consecutive runs (Figure S24a). The MOF crystallinity is kept well after the reaction (Figure S25). Moreover, the PdAg nanocages remain intact and monodispersed thanks to the protection of the MOF shell in the yolk−shell PdAg@ZIF-8 after catalysis (Figure S26). By contrast, the PdAg nanocages present serious aggregation (Figure S12), resulting in inferior recycling performance in the recycling experiments (Figure S24b).

Encouraged by the outstanding catalytic performance of yolk−shell PdAg@ZIF-8 for *para*-nitrostyrene, the selective hydrogenation of *meta*-nitrostyrene and *para*-nitrophenylacetylene under light irradiation has been investigated (Table S4). Delightedly, the transformation of *meta*-nitrostyrene can be completed with excellent selectivity (94%), indicating that the selective hydrogenation of the $-NO_2$ group in the presence of the −C═C bond over PdAg@ZIF-8 is not disturbed by the relative position of the reducible group. Moreover, the hydrogenation of *para*-nitrophenylacetylene displays complete conversion with 85% selectivity to *para*-aminostyrene in 0.5 h and gives almost retained selectivity with a much prolonged reaction time (3 h), further supporting the remarkable selective hydrogenation performance of yolk−shell PdAg@ZIF-8.

CONCLUSIONS

In summary, the yolk−shell structured PdAg@ZIF-8 composite has been developed for efficient and selective hydrogenation of nitrostyrene to aminostyrene at ambient temperature under visible light irradiation. Pd behaves as the main active sites, plasmonic Ag improves the selective adsorption of

https://doi.org/10.1021/jacs.2c06720
J. Am. Chem. Soc. 2022, 144, 17075−17085

the $-NO_2$ group for high selectivity, the photothermal effect of PdAg nanocages further promotes the efficiency, and the MOF shell not only exerts heat preservation but also protects PdAg nanocages from aggregation for recyclability, which cooperates together to guarantee the excellent catalytic performance. The light-induced near-field enhancement around PdAg and the regulated Pd electronic state by Ag alloying benefit the selective adsorption of the $-NO_2$ group over yolk−shell PdAg@ZIF-8. Moreover, the generated polar hydrogen species from NH_3BH_3 suppresses the hydrogenation of the −C═C bond, partially contributing to the resulting selectivity. In addition, the hollow space in the yolk−shell nanostructure has been demonstrated to be essential to the preferential adsorption for $-NO_2$ rather than the −C═C group, which is not achievable by the core−shell PdAg@ZIF-8. This work not only manifests the advantages of light-induced near-field enhancement and yolk−shell nanostructure toward selective catalysis but also integrates synergistic functions of each component in a composite catalyst and opens a new avenue to harnessing solar energy into high-performance heterogeneous catalysis.

MATERIALS AND METHODS

Materials and Equipment. All chemicals were obtained from commercial sources without further purification, unless otherwise stated. XRD was recorded on a Japan Rigaku SmartLab rotation anode X-ray diffractometer equipped with graphite monochromatized Cu Kα radiation (λ = 1.54 Å). TEM and HRTEM images were obtained from a JEOL-2010 with an electron acceleration energy of 200 kV. Nitrogen sorption isotherms were investigated using an automatic volumetric adsorption device (Micrometritics ASAP 2020). Before the gas adsorption/desorption measurement, the samples were entirely dried and activated at 393 K for 24 h. UV−Vis absorption spectra were carried out on a Shimadzu UV-2700 spectrophotometer. The contents of Pd and Ag were estimated using an Optima 7300 DV inductively coupled plasma atomic emission spectrometer (ICP-AES). All of the DRIFTS experiments were carried out over the samples on a Nicolet iS10 spectrometer equipped with a mercury cadmium telluride (MCT) detector and a low-temperature reaction chamber (Praying Mantis Harrick). Prior to the measurement, the sample was sufficiently activated at 393 K for 24 h to eliminate solvent or other adsorbates and enable the adsorption sites exposed. Upon the activation treatment, a certain amount of the sample powder was placed into the reflectance cell and first heated at 120 °C in the 10% H_2/Ar gas atmosphere, followed by cooling down to room temperature in the Ar gas atmosphere. Then, the samples were purged by flowing Ar (25 mL/min) to get a stable background spectrum. Then, the mixture stream of nitrobenzene and styrene loaded in Ar was carried into the sample cell at a rate of 25 mL/min until saturation. The spectra were collected for 256 scans at 4 cm^{-1} resolution. The visible light was provided by a Xe lamp (Perfectlight, PLS-SXE300) with a 400 nm cutoff filter. The thermal images were recorded on a thermograph (HIKVISION, DS-2TPH36). All of the products were obtained from the catalytic reaction and identified and analyzed by gas chromatography (GC, Shimadzu 2014), further determined by an Agilent Technologies 7890A GC with a detector of an Agilent Technologies 5975C mass spectrometer. X-ray photoelectron spectroscopy (XPS) measurements were performed by an ESCALAB 250 high-performance electron spectrometer using the excitation source of monochromatized Al Kα ($h\nu$ = 1486.7 eV). The SRPES spectra were measured with photon energies of 470, 670, 970, and 1486.6 eV at the BL10B beamline in the National Synchrotron Radiation Laboratory (NSRL, Hefei, China). Mercury intrusion pore measurement was carried out on the automatic mercury injection equipment (Microactive Autopore V 9600 version).

Synthesis of Ag Nanocubes. Ag nanocubes were synthesized with a polyol protocol as extensively reported with modifications.[64] In a typical synthesis, 50 mL of ethylene glycol (EG) was added into a 250 mL flask and heated up to 150 °C under stirring in an oil bath. When the temperature reached 150 °C, 600 μL of NaHS (3 mM in EG) was quickly added into the heated solution. After 4 min, the HCl solution (3 mM in EG, 5 mL) and PVP solution (20 mg/mL in EG, 12.5 mL) were injected into the mixture in sequence. After 2 min, the CF_3COOAg solution (282 mM in EG, 4 mL) was injected into the flask. The final solution was further heated at 150 °C for 1 h. During the process, the flask was sealed with a glass stopper, except for the addition of reagents. Finally, the reaction solution was quenched by quickly moving the flask into ice water. The gray Ag nanocubes were collected via centrifugation and washed with acetone and water several times and then redispersed in 25 mL of deionized water (~0.7 mg/mL).

Synthesis of PdAg Nanocages. The PdAg nanocages were obtained through galvanic replacement.[65] Typically, 5.5 mg of the obtained Ag nanocubes were mixed with 50 mg of PVP in the presence of 50 mL of deionized water. The mixture was heated at 90 °C for 20 min. Then, 10 mL of K_2PdCl_4 aqueous solution (0.5 mM) was injected into the heated solution with an automatic sampler at a rate of 0.25 mL/min. Once the injection was finished, the reaction solution was quickly quenched by moving the flask into ice water. The final PdAg nanocages were obtained by centrifugation and washed with saturated NaCl aqueous solution and deionized water three times. The precipitate was redispersed in 5 mL of deionized water. The default Pd and Ag contents were measured to be 9.6 and 90.4 wt %, respectively, in PdAg nanocages by ICP-AES, where the molar ratio of Pd/Ag is ~1/9. When the amount of K_2PdCl_4 aqueous solution was increased to 25 mL, the Pd and Ag contents were measured to be 29.5 and 70.5 wt %, respectively, in PdAg nanocages, where the molar ratio of Pd/Ag is ~3/7.

Coating of Cuprous Oxide onto PdAg Nanocages. The Cu_2O shell on PdAg nanocages was synthesized by modifying a protocol in the literature.[44] Typically, 1 mL of $CuCl_2$ (0.1 M) was diluted with 93.5 mL of deionized water, followed by the addition of PdAg nanocages (1 mL) prepared above. Then, 2.5 mL of NaOH (1 M) was added drop by drop. After the solution was shaken for 10 s, 2 mL of $NH_2OH{\cdot}HCl$ (0.2 M) was added with shaking for 10 s. The solution was aged for 2 h at room temperature. To collect the products, the solution was centrifuged at 5000 rpm for 3 min and then washed with methanol three times. Finally, the precipitation was redispersed in 2 mL of methanol.

Synthesis of Yolk−Shell PdAg@ZIF-8 Composite. Typically, 32.5 mg of $Zn(NO_3)_2$ was dissolved in 1.576 mL of methanol. The obtained solution was stirred in an ice bath. Then, 2 mL of PdAg@Cu_2O methanol solution containing 2-methylimidazole (82.5 mg) was poured to the $Zn(NO_3)_2$ solution quickly. After stirring for 2 h in the ice bath, the solution was kept stirring for one more hour at room temperature. The product was collected by centrifugation and washed three times with methanol. To ensure the removal of the residual Cu_2O, the precipitation was dispersed in 3% ammonium hydroxide/methanol (2 mL) and soaked for 30 min. After the removal process, PdAg@ZIF-8 was harvested via centrifugation and washed with methanol three times. Pd_3Ag_7@ZIF-8 was synthesized with a similar procedure to that of PdAg@ZIF-8, except for using PdAg nanocages with a higher Pd content of 29.5 wt % instead of the default PdAg nanocages with 9.6 wt % Pd loading.

Synthesis of Core−Shell PdAg@ZIF-8. The core−shell PdAg@ZIF-8 was synthesized by the following steps. The as-synthesized PdAg nanocages were dispersed in 5 mL of methanol. Then, 1 mL of the PdAg nanocage methanol solution was taken out and mixed with 50 mL of 2-methylimidazole (25 mM in methanol) and 50 mL of $Zn(NO_3)_2{\cdot}6H_2O$ (25 mM in methanol). The mixture was left still at room temperature for 24 h. The solution was collected by centrifugation and washed with methanol three times. The contents of Pd and Ag in the core−shell PdAg@ZIF-8 are 0.46 and 4.3 wt %, respectively, where the molar ratio of Pd/Ag is ~1/9, based on the ICP-AES data.

Synthesis of Yolk−Shell Ag@ZIF-8. The yolk−shell Ag@ZIF-8 was prepared with similar procedures to that of yolk−shell PdAg@

https://doi.org/10.1021/jacs.2c06720
J. Am. Chem. Soc. 2022, 144, 17075−17085

ZIF-8, except for replacing the 1 mL of PdAg nanocage aqueous solution with 1 mL of Ag nanocube aqueous solution (0.5 mg/mL).

Synthesis of Pd Nanocubes (17 ± 3 nm). The synthesis was carried out according to the previous procedures with modifications.[66] Typically, 105 mg of PVP, 60 mg of L-ascorbic acid, and 600 mg of KBr were dissolved in 8 mL of deionized water in a 20 mL vial. Then, the mixture was heated at 80 °C for 15 min under stirring. After that, 57 mg of K2PdCl4 dissolving in 3 mL of water was added to the solution via a pipette. The reaction mixture was kept aging at 80 °C for 3 h. The final Pd nanocubes were collected by centrifugation and washed three times with water.

Synthesis of Yolk−Shell Pd@ZIF-8. The yolk−shell Pd@ZIF-8 was synthesized following a similar procedure to that of yolk−shell PdAg@ZIF-8, except for replacing 1 mL of PdAg nanocage aqueous solution with 1 mL of Pd nanocube aqueous solution (0.5 mg/mL).

Synthesis of PdAg/C, PdAg/SiO_2, PdAg/Al_2O_3, or PdAg@C. The supported catalysts were prepared by the following steps. First, the as-synthesized PdAg nanocages were dispersed in 5 mL of methanol. Then, 1 mL of methanol solution of the PdAg nanocages was taken out and mixed with 100 mg of PVP (∼55000) stirring for 2 h at room temperature. After that, 50 mg of carbon powder (or SiO_2 powder or neutral Al_2O_3) was added and stirred for 12 h. The final supported catalysts were collected by centrifugation, washed three times with methanol, and dried overnight. PdAg@C was obtained by the following steps. At the beginning, 80 μL of ammonium hydroxide was added into the PdAg@Cu_2O solvent (2 mL) and soaked for 30 min to remove the Cu_2O coating. After centrifugation, the obtained precipitation was dissolved in 1 mL of methanol and mixed with 100 mg of PVP (∼55,000) by stirring for 2 h at room temperature. After that, 50 mg of carbon powder was added and stirred for 12 h. The final catalyst was centrifuged, washed three times with methanol, and dried overnight.

Chemoselective Hydrogenation of Nitrostyrene. Typically, 5 mL of ethanol containing 0.1 mmol of nitrostyrene and 5.5 mg of yolk−shell PdAg@ZIF-8 (the molar ratio of Pd/Ag = 1:9) catalyst were added into a glass tube. The tube was sealed with a rubber stopper, followed by N_2 bubbling for 15 min to form an inert atmosphere inside. Then, 0.5 mL of ethanol dissolving 15 mg of NH_3BH_3 was injected into the mixture rapidly. The obtained solution was stirred continuously for 20 min in the dark or irradiated by a Xe lamp at 300 mW/cm^2 with a 400 nm cutoff filter. After the reaction completion, 200 μL of the resultant mixture was taken into 1 mL of ethyl acetate. Upon adequate shaking, the mixture was allowed to be centrifuged. Then, the upper solution was detected by GC. For the catalytic recycling experiments, PdAg@ZIF-8 was separated by centrifugation after the reaction and washed with ethanol three times before the next run. For controlled experiments, the catalytic performance of Ag@ZIF-8, Pd@ZIF-8, Pd_3Ag_7@ZIF-8, and core−shell structured PdAg@ZIF-8 was also examined under the same conditions otherwise stated.

Computational Details. All DFT calculations were performed with the first-principles method in the Vienna Ab initio Simulation Package (VASP) using a projector augmented wave (PAW) method.[67] The generalized gradient approximation (GGA) with the Perdew−Burke−Ernzerhof (PBE) functional was utilized to treat the electronic exchange−correlation interactions.[68] The spin polarization was taken into consideration to obtain accurate ground-state energy. The DFT-D3 method proposed by Grimme et al. was used to the correct van Der Waals interaction.[69] The Brillouin zone was sampled with a γ point grid, and the kinetic energy cutoff for the plane-wave basis set was determined to be 450 eV. For structural optimization, the positions of the bottom two layers were fixed and other atoms were allowed us to fully relax until the maximum force on any atom was below 0.05 eV/Å. Adsorption energy is considered, where the deformation energy is ignored to better exhibit intrinsic binding strength. The four-layer slab model was constructed based on the Ag(100) surface, and a 15 Å vacuum layer thickness was placed to simulate the surface reaction location. Six palladium atoms are dispersed into the top three layers to show the doping effect of palladium into Ag.

■ ASSOCIATED CONTENT

Supporting Information

The Supporting Information is available free of charge at https://pubs.acs.org/doi/10.1021/jacs.2c06720.

Details on ligand preparation, characterization data, and figures (PDF)

■ AUTHOR INFORMATION

Corresponding Authors

Yu-Jia Zeng − *Key Laboratory of Optoelectronic Devices and Systems of Ministry of Education and Guangdong Province, College of Physics and Optoelectronic Engineering, Shenzhen University, Shenzhen 518060, P. R. China;* orcid.org/0000-0001-5673-3447; Email: yjzeng@szu.edu.cn

Hai-Long Jiang − *Department of Chemistry, University of Science and Technology of China, Hefei, Anhui 230026, P. R. China;* orcid.org/0000-0002-2975-7977; Email: jianglab@ustc.edu.cn

Authors

Luyan Li − *Key Laboratory of Optoelectronic Devices and Systems of Ministry of Education and Guangdong Province, College of Physics and Optoelectronic Engineering, Shenzhen University, Shenzhen 518060, P. R. China; Department of Chemistry, University of Science and Technology of China, Hefei, Anhui 230026, P. R. China*

Yanxiao Li − *Department of Chemistry, University of Science and Technology of China, Hefei, Anhui 230026, P. R. China*

Long Jiao − *Department of Chemistry, University of Science and Technology of China, Hefei, Anhui 230026, P. R. China*

Xiaoshuo Liu − *Key Laboratory of Energy Thermal Conversion and Control of Ministry of Education, School of Energy and Environment, Southeast University, Nanjing, Jiangsu 210096, P. R. China*

Zhentao Ma − *National Synchrotron Radiation Laboratory (NSRL), University of Science and Technology of China, Hefei, Anhui 230029, P. R. China*

Xusheng Zheng − *National Synchrotron Radiation Laboratory (NSRL), University of Science and Technology of China, Hefei, Anhui 230029, P. R. China*

Complete contact information is available at: https://pubs.acs.org/10.1021/jacs.2c06720

Author Contributions

All authors have given approval to the final version of the manuscript.

Notes

The authors declare no competing financial interest.

■ ACKNOWLEDGMENTS

This work was supported by the National Key Research and Development Program of China (2021YFA1500402), the NSFC (21725101, 21871244, and 22161142001), International Partnership Program of CAS (211134KYSB20190109), Collaborative Innovation Program of Hefei Science Center, CAS (2020HSC-CIP005), the Guangdong Basic and Applied Basic Research Foundation (2022A1515010649), and the Shenzhen Science and Technology Project (JCYJ20180507182246321 and JCYJ20210324095611032).

REFERENCES

(1) Jagadeesh, R. V.; Surkus, A.-E.; Junge, H.; Pohl, M.-M.; Radnik, J.; Rabeah, J.; Huan, H.; Schünemann, V.; Brückner, A.; Beller, M. Nanoscale Fe_2O_3-Based Catalysts for Selective Hydrogenation of Nitroarenes to Anilines. *Science* **2013**, *342*, 1073−1076.

(2) Wei, H.; Liu, X.; Wang, A.; Zhang, L.; Qiao, B.; Yang, X.; Huang, Y.; Miao, S.; Liu, J.; Zhang, T. FeO_x-Supported Platinum Single-Atom and Pseudo-Single-Atom Catalysts for Chemoselective Hydrogenation of Functionalized Nitroarenes. *Nat. Commun.* **2014**, *5*, No. 5634.

(3) Ji, P.; Manna, K.; Lin, Z.; Feng, X.; Urban, A.; Song, Y.; Lin, W. Single-Site Cobalt Catalysts at New $Zr_{12}(\mu_3\text{-}O)_8(\mu_3\text{-}OH)_8(\mu_2\text{-}OH)_6$ Metal−Organic Framework Nodes for Highly Active Hydrogenation of Nitroarenes, Nitriles, and Isocyanides. *J. Am. Chem. Soc.* **2017**, *139*, 7004−7011.

(4) Jagadeesh, R. V.; Murugesan, K.; Alshammari, A. S.; Neumann, H.; Pohl, M.-M.; Radnik, J.; Beller, M. MOF-Derived Cobalt Nanoparticles Catalyze a General Synthesis of Amines. *Science* **2017**, *358*, 326−332.

(5) Lin, L.; Yao, S.; Gao, R.; Liang, X.; Yu, Q.; Deng, Y.; Liu, J.; Peng, M.; Jiang, Z.; Li, S.; Li, Y. W.; Wen, X. D.; Zhou, W.; Ma, D. A Highly Co-Tolerant Atomically Dispersed Pt Catalyst for Chemoselective Hydrogenation. *Nat. Nanotechnol.* **2019**, *14*, 354−361.

(6) Murugesan, K.; Senthamarai, T.; Chandrashekhar, V. G.; Natte, K.; Kamer, P. C. J.; Beller, M.; Jagadeesh, R. V. Catalytic Reductive Aminations Using Molecular Hydrogen for Synthesis of Different Kinds of Amines. *Chem. Soc. Rev.* **2020**, *49*, 6273−6328.

(7) Wang, Y.; Qin, R.; Wang, Y.; Ren, J.; Zhou, W.; Li, L.; Ming, J.; Zhang, W.; Fu, G.; Zheng, N. Chemoselective Hydrogenation of Nitroaromatics at the Nanoscale Iron(III)-OH-Platinum Interface. *Angew. Chem., Int. Ed.* **2020**, *59*, 12736−12740.

(8) Vilé, G.; Albani, D.; Nachtegaal, M.; Chen, Z.; Dontsova, D.; Antonietti, M.; Lopez, N.; Perez-Ramirez, J. A Stable Single-Site Palladium Catalyst for Hydrogenations. *Angew. Chem., Int. Ed.* **2015**, *54*, 11265−11269.

(9) Chen, X.; Shen, K.; Ding, D.; Chen, J.; Fan, T.; Wu, R.; Li, Y. Solvent-Driven Selectivity Control to Either Anilines or Dicyclohexylamines in Hydrogenation of Nitroarenes over a Bifunctional Pd/MIL-101 Catalyst. *ACS Catal.* **2018**, *8*, 10641−10648.

(10) Furukawa, S.; Yoshida, Y.; Komatsu, T. Chemoselective Hydrogenation of Nitrostyrene to Aminostyrene over Pd- and Rh-Based Intermetallic Compounds. *ACS Catal.* **2014**, *4*, 1441−1450.

(11) Zhang, J.; Wang, L.; Shao, Y.; Wang, Y.; Gates, B. C.; Xiao, F. S. A Pd@Zeolite Catalyst for Nitroarene Hydrogenation with High Product Selectivity by Sterically Controlled Adsorption in the Zeolite Micropores. *Angew. Chem., Int. Ed.* **2017**, *56*, 9747−9751.

(12) Li, L.; Li, Z.; Yang, W.; Huang, Y.; Huang, G.; Guan, Q.; Dong, Y.; Lu, J.; Yu, S.-H.; Jiang, H.-L. Integration of Pd Nanoparticles with Engineered Pore Walls in MOFs for Enhanced Catalysis. *Chem* **2021**, *7*, 686−698.

(13) Zhang, S.; Chang, C. R.; Huang, Z. Q.; Li, J.; Wu, Z.; Ma, Y.; Zhang, Z.; Wang, Y.; Qu, Y. High Catalytic Activity and Chemoselectivity of Sub-Nanometric Pd Clusters on Porous Nanorods of CeO_2 for Hydrogenation of Nitroarenes. *J. Am. Chem. Soc.* **2016**, *138*, 2629−2637.

(14) Zheng, J.; Cheng, X.; Zhang, H.; Bai, X.; Ai, R.; Shao, L.; Wang, J. Gold Nanorods: the Most Versatile Plasmonic Nanoparticles. *Chem. Rev.* **2021**, *121*, 13342−13453.

(15) Acharya, A.; Dubbu, S.; Kumar, S.; Kumari, N.; Kim, Y.; So, S.; Kwon, T.; Wang, Z.; Park, J.; Cho, Y. K.; Rho, J.; Oh, S. H.; Kumar, A.; Lee, I. S. Atomically Conformal Metal Laminations on Plasmonic Nanocrystals for Efficient Catalysis. *J. Am. Chem. Soc.* **2021**, *143*, 10582−10589.

(16) Wang, F.; Li, C.; Chen, H.; Jiang, R.; Sun, L.-D.; Li, Q.; Wang, J.; Yu, J. C.; Yan, C.-H. Plasmonic Harvesting of Light Energy for Suzuki Coupling Reactions. *J. Am. Chem. Soc.* **2013**, *135*, 5588−5601.

(17) Feng, J.; Yang, F.; Wang, X.; Lyu, F.; Li, Z.; Yin, Y. Self-Aligned Anisotropic Plasmonic Nanostructures. *Adv. Mater.* **2019**, *31*, No. e1900789.

(18) Aslam, U.; Rao, V. G.; Chavez, S.; Linic, S. Catalytic Conversion of Solar to Chemical Energy on Plasmonic Metal Nanostructures. *Nat. Catal.* **2018**, *1*, 656−665.

(19) Li, L.; Yang, W.; Yang, Q.; Guan, Q.; Lu, J.; Yu, S.-H.; Jiang, H.-L. Accelerating Chemo- and Regioselective Hydrogenation of Alkynes over Bimetallic Nanoparticles in a Metal−Organic Framework. *ACS Catal.* **2020**, *10*, 7753−7762.

(20) Chen, Y. Z.; Wang, Z. U.; Wang, H.; Lu, J.; Yu, S. H.; Jiang, H.-L. Singlet Oxygen-Engaged Selective Photo-Oxidation over Pt Nanocrystals/Porphyrinic MOF: The Roles of Photothermal Effect and Pt Electronic State. *J. Am. Chem. Soc.* **2017**, *139*, 2035−2044.

(21) Chow, T. H.; Li, N.; Bai, X.; Zhuo, X.; Shao, L.; Wang, J. Gold Nanobipyramids: an Emerging and Versatile Type of Plasmonic Nanoparticles. *Acc. Chem. Res.* **2019**, *52*, 2136−2146.

(22) Linic, S.; Chavez, S.; Elias, R. Flow and Extraction of Energy and Charge Carriers in Hybrid Plasmonic Nanostructures. *Nat. Mater.* **2021**, *20*, 916−924.

(23) Lin, R.; Hu, L.; Wang, J.; Zhang, W.; Ruan, S.; Zeng, Y. J. Raman Scattering Enhancement of a Single Zno Nanorod Decorated with Ag Nanoparticles: Synergies of Defects and Plasmons. *Opt. Lett.* **2018**, *43*, 2244−2247.

(24) Hu, F.; Abeyweera, S. C.; Yu, J.; Zhang, D.; Wang, Y.; Yan, Q.; Sun, Y. Quantifying Electrocatalytic Reduction of CO_2 on Twin Boundaries. *Chem* **2020**, *6*, 3007−3021.

(25) Cai, G.; Ding, M.; Wu, Q.; Jiang, H. L. Encapsulating Soluble Active Species into Hollow Crystalline Porous Capsules Beyond Integration of Homogeneous and Heterogeneous Catalysis. *Natl. Sci. Rev.* **2020**, *7*, 37−45.

(26) Furukawa, H.; Cordova, K. E.; O'Keeffe, M.; Yaghi, O. M. The Chemistry and Applications of Metal-Organic Frameworks. *Science* **2013**, *341*, No. 1230444.

(27) Zhou, H. C.; Kitagawa, S. Metal-Organic Frameworks (MOFs). *Chem. Soc. Rev.* **2014**, *43*, 5415−5418.

(28) Li, B.; Wen, H.-M.; Cui, Y.; Zhou, W.; Qian, G.; Chen, B. Emerging Multifunctional Metal-Organic Framework Materials. *Adv. Mater.* **2016**, *28*, 8819−8860.

(29) Islamoglu, T.; Goswami, S.; Li, Z.; Howarth, A. J.; Farha, O. K.; Hupp, J. T. Postsynthetic Tuning of Metal-Organic Frameworks for Targeted Applications. *Acc. Chem. Res.* **2017**, *50*, 805−813.

(30) Jiao, L.; Wang, J.; Jiang, H.-L. Microenvironment Modulation in Metal−Organic Framework-Based Catalysis. *Acc. Mater. Res.* **2021**, *2*, 327−339.

(31) Zhao, X.; Wang, Y.; Li, D.-S.; Bu, X.; Feng, P. Metal-Organic Frameworks for Separation. *Adv. Mater.* **2018**, *30*, No. 1705189.

(32) Zhang, W.; Wang, L.; Wang, K.; Khan, M. U.; Wang, M.; Li, H.; Zeng, J. Integration of Photothermal Effect and Heat Insulation to Efficiently Reduce Reaction Temperature of CO_2 Hydrogenation. *Small* **2017**, *13*, No. 1602583.

(33) Yang, Q.; Xu, Q.; Yu, S.-H.; Jiang, H.-L. Pd Nanocubes@ZIF-8: Integration of Plasmon-Driven Photothermal Conversion with a Metal-Organic Framework for Efficient and Selective Catalysis. *Angew. Chem., Int. Ed.* **2016**, *55*, 3685−3689.

(34) Qi, L.; Chen, J.; Zhang, B.; Nie, R.; Qi, Z.; Kobayashi, T.; Bao, Z.; Yang, Q.; Ren, Q.; Sun, Q.; Zhang, Z.; Huang, W. Deciphering a Reaction Network for The Switchable Production of Tetrahydroquinoline or Quinoline with MOF-Supported Pd Tandem Catalysts. *ACS Catal.* **2020**, *10*, 5707−5714.

(35) Yang, Q.; Xu, Q.; Jiang, H.-L. Metal-Organic Frameworks Meet Metal Nanoparticles: Synergistic Effect for Enhanced Catalysis. *Chem. Soc. Rev.* **2017**, *46*, 4774−4808.

(36) Kobayashi, H.; Taylor, J. M.; Mitsuka, Y.; Ogiwara, N.; Yamamoto, T.; Toriyama, T.; Matsumura, S.; Kitagawa, H. Charge Transfer Dependence on CO_2 Hydrogenation Activity to Methanol in Cu Nanoparticles Covered with Metal-Organic Framework Systems. *Chem. Sci.* **2019**, *10*, 3289−3294.

(37) Fang, C.; Liu, L.; Weng, J.; Zhang, S.; Zhang, X.; Ren, Z.; Shen, Y.; Meng, F.; Zheng, B.; Li, S.; Wu, J.; Shi, W.; Lee, S.; Zhang, W.; Huo, F. Modifiers versus Channels: Creating Shape-Selective

https://doi.org/10.1021/jacs.2c06720
J. Am. Chem. Soc. 2022, 144, 17075−17085

Catalysis of Metal Nanoparticles/Porous Nanomaterials. *Angew. Chem., Int. Ed.* **2021**, *60*, 976−982.
(38) Li, G.; Zhao, S.; Zhang, Y.; Tang, Z. Metal-Organic Frameworks Encapsulating Active Nanoparticles as Emerging Composites for Catalysis: Recent Progress and Perspectives. *Adv. Mater.* **2018**, *30*, No. 1800702.
(39) Chen, L.; Luque, R.; Li, Y. Controllable Design of Tunable Nanostructures Inside Metal-Organic Frameworks. *Chem. Soc. Rev.* **2017**, *46*, 4614−4630.
(40) Park, K. S.; Ni, Z.; Cote, A. P.; Choi, J. Y.; Huang, R.; Uribe-Romo, F. J.; Chae, H. K.; O'Keeffe, M.; Yaghi, O. M. Exceptional Chemical and Thermal Stability of Zeolitic Imidazolate Frameworks. *Proc. Natl. Acad. Sci. U.S.A.* **2006**, *103*, 10186−10191.
(41) Huang, X. C.; Lin, Y. Y.; Zhang, J. P.; Chen, X. M. Ligand-Directed Strategy for Zeolite-Type Metal-Organic Frameworks: Zinc(II) Imidazolates with Unusual Zeolitic Topologies. *Angew. Chem., Int. Ed.* **2006**, *45*, 1557−1559.
(42) Siekkinen, A. R.; McLellan, J. M.; Chen, J.; Xia, Y. Rapid Synthesis of Small Silver Nanocubes by Mediating Polyol Reduction with a Trace Amount of Sodium Sulfide or Sodium Hydrosulfide. *Chem. Phys. Lett.* **2006**, *432*, 491−496.
(43) Zhao, X.; Long, R.; Liu, D.; Luo, B.; Xiong, Y. Pd−Ag Alloy Nanocages: Integration of Ag Plasmonic Properties with Pd Active Sites for Light-Driven Catalytic Hydrogenation. *J. Mater. Chem. A* **2015**, *3*, 9390−9394.
(44) Kuo, C. H.; Tang, Y.; Chou, L. Y.; Sneed, B. T.; Brodsky, C. N.; Zhao, Z.; Tsung, C. K. Yolk-Shell Nanocrystal@ZIF-8 Nanostructures for Gas-Phase Heterogeneous Catalysis with Selectivity Control. *J. Am. Chem. Soc.* **2012**, *134*, 14345−14348.
(45) Chen, Y.-Z.; Zhou, Y.-X.; Wang, H.; Lu, J.; Uchida, T.; Xu, Q.; Yu, S.-H.; Jiang, H.-L. Multifunctional PdAg@MIL-101 for One-pot Cascade Reactions: Combination of Host−Guest Cooperation and Bimetallic Synergy in Catalysis. *ACS Catal.* **2015**, *5*, 2062−2069.
(46) Shen, M.; Liu, H.; Yu, C.; Yin, Z.; Muzzio, M.; Li, J.; Xi, Z.; Yu, Y.; Sun, S. Room-Temperature Chemoselective Reduction of 3-Nitrostyrene to 3-Vinylaniline by Ammonia Borane over Cu Nanoparticles. *J. Am. Chem. Soc.* **2018**, *140*, 16460−16463.
(47) Li, J.; Long, Y.; Liu, Y.; Zhang, L.; Wang, Q.; Wang, X.; Song, S.; Zhang, H. Robust Synthesis of Gold-Based Multishell Structures as Plasmonic Catalysts for Selective Hydrogenation of 4-Nitrostyrene. *Angew. Chem., Int. Ed.* **2020**, *59*, 1103−1107.
(48) Yang, Q.; Chen, Y. Z.; Wang, Z. U.; Xu, Q.; Jiang, H.-L. One-Pot Tandem Catalysis Over Pd@MIL-101: Boosting the Efficiency of Nitro Compound Hydrogenation by Coupling with Ammonia Borane Dehydrogenation. *Chem. Commun.* **2015**, *51*, 10419−10422.
(49) Zhan, W.-W.; Zhu, Q.-L.; Xu, Q. Dehydrogenation of Ammonia Borane by Metal Nanoparticle Catalysts. *ACS Catal.* **2016**, *6*, 6892−6905.
(50) Han, C.; Meng, P.; Waclawik, E. R.; Zhang, C.; Li, X. H.; Yang, H.; Antonietti, M.; Xu, J. Palladium/Graphitic Carbon Nitride ($G\text{-}C_3N_4$) Stabilized Emulsion Microreactor as a Store for Hydrogen from Ammonia Borane for Use in Alkene Hydrogenation. *Angew. Chem., Int. Ed.* **2018**, *57*, 14857−14861.
(51) Sim, H. Y. F.; Lee, H. K.; Han, X.; Koh, C. S. L.; Phan-Quang, G. C.; Lay, C. L.; Kao, Y. C.; Phang, I. Y.; Yeow, E. K. L.; Ling, X. Y. Concentrating Immiscible Molecules at Solid@MOF Interfacial Nanocavities to Drive an Inert Gas-Liquid Reaction at Ambient Conditions. *Angew. Chem., Int. Ed.* **2018**, *57*, 17058−17062.
(52) Fang, Y.; Guan, B. Y.; Luan, D.; Lou, X. W. Synthesis of CuS@CoS_2 Double-Shelled Nanoboxes with Enhanced Sodium Storage Properties. *Angew. Chem., Int. Ed.* **2019**, *58*, 7739−7743.
(53) Wang, J.; Cui, Y.; Wang, D. Design of Hollow Nanostructures for Energy Storage, Conversion and Production. *Adv. Mater.* **2019**, *31*, No. 1801993.
(54) Peiris, E.; Sarina, S.; Waclawik, E. R.; Ayoko, G. A.; Han, P.; Jia, J.; Zhu, H. Y. Plasmonic Switching of the Reaction Pathway: Visible-Light Irradiation Varies the Reactant Concentration at the Solid-Solution Interface of a Gold-Cobalt Catalyst. *Angew. Chem., Int. Ed.* **2019**, *58*, 12032−12036.
(55) Hu, C.; Chen, X.; Jin, J.; Han, Y.; Chen, S.; Ju, H.; Cai, J.; Qiu, Y.; Gao, C.; Wang, C.; Qi, Z.; Long, R.; Song, L.; Liu, Z.; Xiong, Y. Surface Plasmon Enabling Nitrogen Fixation in Pure Water Through a Dissociative Mechanism under Mild Conditions. *J. Am. Chem. Soc.* **2019**, *141*, 7807−7814.
(56) Hallock, A. J.; Redmond, P. L.; Brus, L. E. Optical Forces Between Metallic Particles. *Proc. Natl. Acad. Sci. U.S.A.* **2005**, *102*, 1280−1284.
(57) Osborne, M. A.; Balasubramanian, S.; Furey, W. S.; Klenerman, D. Optically Biased Diffusion of Single Molecules Studied by Confocal Fluorescence Microscopy. *J. Phys. Chem. B* **1998**, *102*, 3160−3167.
(58) Tong, F.; Liang, X.; Ma, F.; Bao, X.; Wang, Z.; Liu, Y.; Wang, P.; Cheng, H.; Dai, Y.; Huang, B.; Zheng, Z. Plasmon-Mediated Nitrobenzene Hydrogenation with Formate as the Hydrogen Donor Studied at a Single-Particle Level. *ACS Catal.* **2021**, *11*, 3801−3809.
(59) Han, P.; Tana, T.; Xiao, Q.; Sarina, S.; Waclawik, E. R.; Gómez, D. E.; Zhu, H. Promoting Ni(II) Catalysis with Plasmonic Antennas. *Chem* **2019**, *5*, 2879−2899.
(60) Zhang, W.; Zheng, B.; Shi, W.; Chen, X.; Xu, Z.; Li, S.; Chi, Y. R.; Yang, Y.; Lu, J.; Huang, W.; Huo, F. Site-Selective Catalysis of a Multifunctional Linear Molecule: the Steric Hindrance of Metal-Organic Framework Channels. *Adv. Mater.* **2018**, *30*, No. e1800643.
(61) Li, Z.; He, T.; Liu, L.; Chen, W.; Zhang, M.; Wu, G.; Chen, P. Covalent Triazine Framework Supported Non-Noble Metal Nanoparticles with Superior Activity for Catalytic Hydrolysis of Ammonia Borane: from Mechanistic Study to Catalyst Design. *Chem. Sci.* **2017**, *8*, 781−788.
(62) Li, L.; Yang, W.; Yang, Q.; Guan, Q.; Lu, J.; Yu, S.-H.; Jiang, H.-L. Accelerating Chemo- and Regioselective Hydrogenation of Alkynes over Bimetallic Nanoparticles in a Metal−Organic Framework. *ACS Catal.* **2020**, *10*, 7753−7762.
(63) Mitsudome, T.; Yamamoto, M.; Maeno, Z.; Mizugaki, T.; Jitsukawa, K.; Kaneda, K. One-Step Synthesis of Core-Gold/Shell-Ceria Nanomaterial and Its Catalysis for Highly Selective Semihydrogenation of Alkynes. *J. Am. Chem. Soc.* **2015**, *137*, 13452−13455.
(64) Li, B.; Long, R.; Zhong, X.; Bai, Y.; Zhu, Z.; Zhang, X.; Zhi, M.; He, J.; Wang, C.; Li, Z. Y.; Xiong, Y. Investigation of Size-Dependent Plasmonic and Catalytic Properties of Metallic Nanocrystals Enabled by Size Control with HCl Oxidative Etching. *Small* **2012**, *8*, 1710−1716.
(65) Xia, X.; Wang, Y.; Ruditskiy, A.; Xia, Y. Galvanic Replacement: a Simple and Versatile Route to Hollow Nanostructures with Tunable and Well-Controlled Properties. *Adv. Mater.* **2013**, *25*, 6313−6333.
(66) Jin, M.; Liu, H.; Zhang, H.; Xie, Z.; Liu, J.; Xia, Y. Synthesis of Pd Nanocrystals Enclosed by {100} Facets and with Sizes <10 nm for Application in CO Oxidation. *Nano Res.* **2010**, *4*, 83−91.
(67) Kresse, G.; Furthmuller, J. Efficiency of Ab-initio Total Energy Calculations for Metals and Semiconductors Using a Plane-Wave Basis Set. *Comput. Mater. Sci.* **1996**, *6*, 15−50.
(68) Kresse, G.; Joubert, D. From Ultrasoft Pseudopotentials to the Projector Augmented-Wave Method. *Phys. Rev. B* **1999**, *59*, 1758−1775.
(69) Grimme, S.; Antony, J.; Ehrlich, S.; Krieg, H. A Consistent and Accurate Ab initio Parametrization of Density Functional Dispersion Correction (DFT-D) for the 94 Elements H-Pu. *J. Chem. Phys.* **2010**, *132*, No. 154104.

https://doi.org/10.1021/jacs.2c06720
J. Am. Chem. Soc. 2022, 144, 17075−17085